Field application of moment-based wavefront sensing to in-situ alignment and image quality assessment of astronomical spectrographs: results and analysis of aligning VIRUS unit spectrographs

Lee, Hanshin, Hill, Gary, Tuttle, Sarah, Noyola, Eva, Peterson, Trent, et al.

Hanshin Lee, Gary J. Hill, Sarah E. Tuttle, Eva Noyola, Trent Peterson, Brian L. Vattiat, "Field application of moment-based wavefront sensing to in-situ alignment and image quality assessment of astronomical spectrographs: results and analysis of aligning VIRUS unit spectrographs," Proc. SPIE 9151, Advances in Optical and Mechanical Technologies for Telescopes and Instrumentation, 91513O (19 August 2014); doi: 10.1117/12.2056706

SPIE.

Event: SPIE Astronomical Telescopes + Instrumentation, 2014, Montréal, Quebec, Canada

Field application of moment-based wavefront sensing to in-situ alignment and image quality assessment of astronomical spectrographs: Results and analysis of aligning VIRUS unit spectrographs

Hanshin Lee, Gary J. Hill, Sarah E. Tuttle, Eva Noyola, Trent Peterson, and Brian L. Vattiat

McDonald Observatory, University of Texas at Austin, 2515 Speedway C1402, Austin, Texas 787127

ABSTRACT

Teague introduced a phase retrieval method that uses the image shape moments. More recently, an independent study arrived at a similar technique, which was then applied to in-situ full-field image-quality evaluation of spectroscopic systems. This moment-based wavefront sensing (MWFS) method relies on the geometric relation between the image shape moments and the geometric wavefront modal coefficients. The MWFS method allows a non-iterative determination of the modal coefficients from focus-modulated images at arbitrary spatial resolutions. The determination of image moments is a direct extension of routine centroid and image size calculation, making its implementation easy. Previous studies showed that the MWFS works well in capturing large low-order modes, and is quite suitable for in-situ alignment diagnostics. At the Astronomical Instrumentation conference in 2012, we presented initial results of the application of the moment-based wavefront sensing to a fiber-fed astronomical spectrograph, called VIRUS (a set of replicated 150 identical integral-field unit spectrographs contained in 75 unit pairs). This initial result shows that the MWFS can provide accurate full-field image-quality assessment for efficiently aligning these 150 spectrographs. Since then, we have assembled more than 24 unit pairs using this technique. In this paper, we detail the technical update/progress made so far for the moment-based wavefront sensing method and the statistical estimates of the before/after alignment aberrations, image-quality, and various efficiency indicators of the unit spectrograph alignment process.

Keywords: Image moment, Wavefront sensing, In situ, Full field image quality, Astronomical Spectrograph, VIRUS instrument

1. INTRODUCTION

The shape of a focus-modulated PSF changes in certain patterns that can be attributed to different wavefront modes. Such shape variation is an excellent tool for visually assessing the image quality of optical systems.[1] Among many PSF shape parameters, the width, ellipticity, and diffraction rings are used to assess focus, astigmatism, and spherical aberrations. However, the PSF can be complex in shape and sampled over a pixel grid much coarser than the diffraction scale. Depending on required accuracy, this can make it challenging to readily measure the aforesaid shape parameters. Alternatively, one can use phase diversity[2] or curvature sensing.[3] Each technique has its own intrinsic strength in particular applications over the other[4] and effort has been made to broaden the application of these techniques.[5–8] Meanwhile, some explored a different approach to focal-plane wavefront sensing, where the dependence of PSF shape on wavefront modes is utilized in the form of a linear relation between the PSF shape moments and wavefront modal coefficients. Teague first recognized this moment-aberration relation in the context of developing the intensity transport equation aspect of phase retrieval problem.[9] Recently, an independent study also recognized the relation in terms of in-situ fine alignment of astronomical spectrographs[10] in developing an in-situ image-quality assessment tool for fast near ultra-violet spectrometers. Both have shown that the linear relation between aberration modes and moments permits non-iterative determination of modal coefficients at various orders. The latter also reported the moment-based sensing accuracy can be comparable to that of typical wavefront sensors. Also noted by Teague and shown elsewhere[11]

Further author information: (Send correspondence to Hanshin Lee)
Hanshin Lee: E-mail: lee@astro.as.utexas.edu, Telephone: 1 512 471 9985

Advances in Optical and Mechanical Technologies for Telescopes and Instrumentation, edited by Ramón Navarro, Colin R. Cunningham, Allison A. Barto, Proc. of SPIE Vol. 9151, 91513O
 doi: 10.1117/12.2056706

is the point source formulation being applicable to extended objects. At the Astronomical Instrumentation conference in 2012, we presented initial results of the application of the moment-based wavefront sensing to a fiber-fed astronomical spectrograph, called the VIRUS instrument (a set of replicated 150 identical integral-field unit spectrographs contained in 75 unit pairs).[12] This initial result shows that the MWFS can provide accurate full-field image-quality assessment for efficiently aligning these 150 spectrographs. Since then, we have assembled more than 24 unit pairs (48 channels) using this technique. In this paper, we detail the technical update/progress (mainly the error propagation analysis) made so far for the moment-based wavefront sensing method and the statistical estimates of the before/after alignment aberrations, image-quality, and various efficiency indicators of the unit spectrograph alignment process. We begin with revisiting the basic theory of the MWFS in Section 2. We then lay out the update on the error propagation analysis in terms of the pixelation error, photon noise, and read-out noise in Section 3. We describe the application to the VIRUS instrument alignment, some statistics and efficiency analysis in Section 4.

2. MOMENT-BASED MODAL WAVEFRONT SENSING THEORY

The MWFS is a new type of modal wavefront sensing technique that utilizes focal-plane images. The sensed quantities are wave aberration coefficients. Compared to the other focal plane wavefront sensing methods, such as the curvature sensing or the iterative phase retrieval procedure, the MWFS differs in the way of utilizing the focal-plane images. The main measurement of the MWFS is the k-th moment of the image of an object. If the image is considered as a 2D distribution of light, the image moments simply tell us about the geometric shape of the distribution. For example, the 1st moment (i.e. centroid) corresponds to the systematic image shift, and the 2nd moment (variance) describes the systematic spread of the distribution. As the order k grows, the finer details of the distribution shape are revealed, e.g. skewness and kurtosis. Measuring moments from an image is merely a simple extension of measuring the centroid or full-width-half-maximum (FWHM) of a point spread function (PSF) and thus can permit rapid WFS.

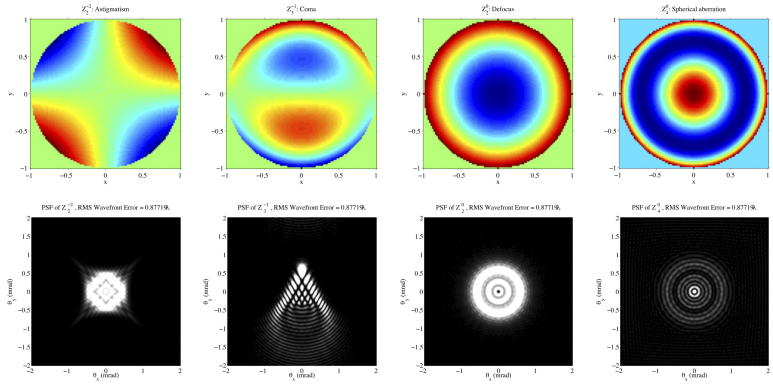

Figure 1. (Top row) Example wavefront aberrations modes and (bottom row) the corresponding point spread functions.

Suppose an ideal optical system free from aberrations. In the geometric approximation, such a system would focus all rays from a point object to a point image. In reality, all optical systems do exhibit some degree of optical aberrations and therefore produce blurred PSFs. As shown in Figure 1, each different aberrations changes the PSF shape in a rather uniquely different way that it is possible to derive some kind of relationship between image shapes and aberration modes. We first describe such relation in the geometric optics limit, but extend it to the wave optics region in the following.

Let $\theta(s,t)$ be the wavefront aberration from a point object at a fixed field and defined over a circular pupil Ω whose coordinate is (s,t). Let θ be expressed as a weighted sum of M Zernike modes (Eq. 1) and W_4 (i.e. the 4th modal coefficient) be modulated as in focusing through a detector.

$$\theta = W_1 Z_1 + W_2 Z_2 + W_3 Z_3 + \cdots + W_M Z_M. \tag{1}$$

Note that Noll's Zernike index scheme is used throughout.[13] θ then results in the ray aberration around the ideal image as,

$$X = -f\,\partial_s\theta = -f\theta_s \;\text{ and }\; Y = -f\,\partial_t\theta = -f\theta_t, \tag{2}$$

where f is the focal length and $\partial_a\theta = \theta_a$ is the partial derivative of θ with respect to a. Note that θ_s and θ_t are linear functions of W_4 and so are X and Y.

The total signal within a section of the focal surface can be given by summing the irradiance of all *geometric* rays landing there. The collection of the signals of these sections forms the PSF whose shape can be characterized by the q-th shape moment as,

$$\mu^g_{nm} = \Big\{ \iint_\Omega I\; X^n\; Y^m \mathrm{d}s\mathrm{d}t \Big\} / \Big\{ \iint_\Omega I\, \mathrm{d}s\mathrm{d}t \Big\}, \tag{3}$$

where I is the irradiance over Ω and q=n+m with $n,m\geq 0$. μ^g_{nm} is the *geometric* version of the PSF shape moment in the pupil plane. In the focal plane,

$$\mu^d_{nm} = \frac{\iint_\Lambda p\; x^n y^m \mathrm{d}x\mathrm{d}y}{\iint_\Lambda p\; \mathrm{d}x\mathrm{d}y} \approx \mathtt{M}_{nm} = \frac{\sum_{k=1}^{N_{px}} p_k x_k^n y_k^m}{\sum_{k=1}^{N_{px}} p_k}, \tag{4}$$

where p is the signal within the PSF region, Λ. $\mathtt{M}_{nm}$ emphasizes that μ^d_{nm} can only be approximated by discrete signal p_k in the k-th pixel at (x_k,y_k).

To the geometric limit, Eq. 3 is equivalent to Eq. 4, but, since p contains diffraction effect, Eq. 4 deviates from Eq. 3 by the amount of diffraction. Following Teague,[9] let $U(s,t)$ and $u(x,y)$ be the pupil and focal plane wave fields, respectively, such that $p = u^\dagger\, u$ and $I = U^\dagger\, U$. $\dagger$ indicates complex conjugate. Due to the Fresnel diffraction approximation,

$$u(x,y) = (i/\lambda\mathtt{f}) \exp\left[-i2\pi\mathtt{f}/\lambda\right] \exp\left[-i\pi(x^2+y^2)/\lambda\mathtt{f}\right]\, g(x/\lambda\mathtt{f}, y/\lambda\mathtt{f}) \tag{5}$$

where $g = \mathtt{FT}[U]$ is the Fourier transform of U. The continuous moment equation in Eq. 4 becomes

$$\mu_{nm} \sim \iint_\Lambda g^\dagger\, x^n\, y^m\, g\, \mathrm{d}x\mathrm{d}y \tag{6}$$

where λ is the wavelength and the normalization is omitted. Using $\mathtt{FT}[\partial_w^n h(w)] = (i2\pi z)^n H(z)$ and Parseval's theorem and assuming total signal in Ω is contained in Λ, Eq. 6 can be re-written in the pupil plane as,

$$\mu_{nm} \sim \iint_\Omega U^\dagger \left(\frac{\partial_s}{i}\right)^n \left(\frac{\partial_t}{i}\right)^m U\; \mathrm{d}s\mathrm{d}t. \tag{7}$$

The integral is the inner product of U to itself with the hermitian derivative operator (similar to the momentum operator[?]), meaning that the integral must be real.

For constant I, the 1^{st} order moments are given as,

$$\mu_{10} = \iint_\Omega I\,(-\mathtt{f}\theta_s)\,\mathrm{d}s\mathrm{d}t,\; \mu_{01} = \iint_\Omega I\,(-\mathtt{f}\theta_t)\,\mathrm{d}s\mathrm{d}t, \tag{8}$$

identical to Eq. 3. The 2^{nd} moments are

$$\mu_{20} = \iint_\Omega I\,\mathtt{f}^2\theta_s^2\,\mathrm{d}s\mathrm{d}t,\; \mu_{11} = \iint_\Omega I\,\mathtt{f}^2\theta_s\theta_t\,\mathrm{d}s\mathrm{d}t. \tag{9}$$

These are also identical to Eq. 3. Among four 3^{rd} order moments, μ_{30} is expressed as,

$$\mu_{30} = \iint_\Omega \left\{ I\left(\frac{\lambda}{2\pi}\right)^2 \mathtt{f}^3\theta_{sss} + I\,(-\mathtt{f}\theta_s)^3 \right\} \mathrm{d}s\mathrm{d}t, \tag{10}$$

where $\theta_{sss} = \partial_s^3\theta$. The first integrand is the diffraction effect and missing in Eq. 3. As the moment order becomes higher, more diffraction terms (with increasingly higher order derivatives of θ) appear. But supposing that θ can be expressed as a linear function of aberration modes in Noll's ordering scheme,[13] the q-th moment becomes a polynomial function of the modal coefficients (W_k) with q being the highest polynomial order. For focus modulation (W_4), the highest order term W_4^q has a constant coefficient, while the next highest order term (W_4^{q-1}) must have its coefficient as a linear combination of some W_k, which is the key to establishing the linear relation between W_k and μ_{nm} as discussed later. This q-1th coefficient (or *the q-1th differential moment*) can is essentially equivalent to $\partial^{q-1}\mu_{nm}/\partial W_4^{q-1}$ (to be called $d\mu_{nm}$). Interestingly, the highest order of diffraction terms turn out to be q-2, i.e. the q-1th differential moment is purely geometric.

In case that I varies in (s,t), μ_{11} is given as,

$$\mu_{11} = \iint_\Omega \left(\frac{\lambda \mathtt{f}}{2\pi i}\right)^2 A\, A_{st} + I(\mathtt{f}\,\theta_s)(\mathtt{f}\theta_t)\,\mathrm{d}s\mathrm{d}t, \tag{11}$$

where imaginary terms are omitted. The first term is due to non-uniform A, but independent of phase, thus the 1st differential moment depends on the second term that is identical to μ_{11} in Eq. 9. For μ_{40}, we have

$$\begin{aligned}\mu_{40} =& \mathtt{f}^4 \iint_\Omega \left(\frac{\lambda}{2\pi}\right)^2 \Big\{ AA_{ssss} - 6AA_{ss}\theta_s^2 - 12AA_s\theta_s\theta_{ss} \\ & -3I\theta_{ss}^2 - 4I\theta_s\theta_{sss}\Big\} + I\theta_s^4 \mathrm{d}s\mathrm{d}t.\end{aligned} \tag{12}$$

Terms in $\{\cdot\}$ are due to non-uniform amplitude and diffraction. The highest order of W_4 in these terms is 2 as discussed. Note that the coefficient of W_4^3 can only be given from the last term due to geometric effect and that the shape of the pupil amplitude plays a role in the differential moment only through the geometric term. The above analysis shows that, in the most general case where both θ and I are as functions of the pupil coordinates, the geometric version of the differential moment is equivalent to the diffractive counterpart.

Turning to a more practical aspect of measuring $d\mu_{nm}$, one needs to obtain N focus-modulated focal plane images and computes the moments of order up to q from those images. The q-1th coefficient of an order q polynomial fit to the modulated moments is used as $d\mu_{nm}$. For the unique polynomial fit, $N \geq q+1$. Note there are q+1 $d\mu_{nm}$ at each order and, up to order q, there are $L = q(q+3)/2$ $d\mu_{nm}$. One can formulate,

$$\vec{u} = \mathbf{M}\vec{W}. \tag{13}$$

$\mathbf{M}$ is a matrix given by the integral in Eq. 3 for W_4^{q-1} terms. $\vec{u}$ and $\vec{W}$ are vectors of $d\mu_{nm}$ and W_k, respectively. Solving Eq. 13 results in the first L W_k (no W_1).

3. ERROR PROPAGATION ANALYSIS

Since the PSF is a photon distribution recorded on a pixelated detector, its shape moment is subject to the pixelation error. Given the total PSF photons (N_{ph}) and letting $p(x,y)$ be the true photon distribution, the photon count (p_k) is the integral of p over at the k-th pixel (Δ_k). By letting $\delta x_k = x - x_k$ and $\delta y_k = y - y_k$ and by expanding the moment kernel $\phi_{nm}(x,y) = x^n y^m$ to a series around (x_k, y_k), μ_{nm} in Eq. 4 can be written as,

$$\mu_{nm} = \frac{1}{N_{ph}} \sum_{k=1}^{N_{px}} \iint_{\Delta_k} p\,\phi_{nm} + p\,(\partial_x\phi_{nm})\,\delta x_k + p\,(\partial_y\phi_{nm})\,\delta y_k + O(\epsilon)\,\mathrm{d}x\mathrm{d}y. \tag{14}$$

Here ϕ_{nm}, $\partial_x\phi_{nm}$, and $\partial_y\phi_{nm}$ are given at (x_k,y_k) and $O(\epsilon)$ includes all higher order terms. The first term is $\mathtt{M}_{nm}$. The rest is the pixelation error (δ_{nm}) of $\mathtt{M}_{nm}$. Expanding p in δ_{nm} into a series within Δ_k leads to,

$$\delta_{nm} \approx -\frac{\Delta^2}{12} \sum_{k=1}^{N_{px}} \frac{\partial_x\phi_{nm}\partial_x p + \partial_y\phi_{nm}\partial_y p}{N_{ph}/\Delta^2}, \tag{15}$$

where Δ is the pixel size. The exact value of δ_{nm} depends on the (unknown) PSF shape. But, one can gain the following insights. The sum can be viewed as a 2-dimensional integral of $\nabla\phi_{nm} \cdot \nabla p$. Like the one in Eq. 4, this integral quantifies the response of ∇p to $\nabla\phi_{nm}$. Intuitively, if p has a strong response to a certain ϕ_{nm} (thus large μ_{nm}), its gradient should respond to the gradient of the same kernel in a similar way if not exactly the same, implying a strong correlation between δ_{nm} and μ_{nm} (e.g. $|\delta_{nm}| \approx 0$ for $|\mu_{nm}| = 0$). Another aspect is $\delta_{nm} \propto \Delta^2$, confirming the known fact that a higher spatial resolution (or N_{px}) leads to a smaller δ_{nm}. Finally, the pixelation error is due to a lack of approximation to the true PSF and thus systematic. In Eq. 15, one may use the numerical gradient of p and ϕ_{nm} to estimate δ_{nm}, but, since ϕ_{nm} is known, a better estimate may be obtained using all derivatives of ϕ_{nm}, as,

$$\delta_{nm} \approx \frac{1}{N_{ph}} \sum_{k=1}^{N_{px}} \left[\sum_{l=1}^{q} \left\{ \sum_{i=0}^{l} \frac{1}{i!j!} \partial_x^i \partial_y^j \phi_{nm} \left(\iint_{\Delta_k} p_0 \mathtt{x}^i \mathtt{y}^j + (\partial_x p)\, \mathtt{x}^{i+1} \mathtt{y}^j + (\partial_y p)\, \mathtt{x}^i \mathtt{y}^{j+1} \mathrm{dxdy} \right) \right\} \right]. \tag{16}$$

Here $j = l - i$, $\mathtt{x} = x_k + x$ and $\mathtt{y} = y_k + y$, and p_0 and all derivatives are evaluated at (x_k, y_k).

Besides the pixelation error, the intrinsic uncertainty of photon detection also imposes Poisson random error $P(\cdot)$ and the imaging detector adds zero mean Gaussian random read noise $G(\cdot)$ to each pixel value, leading to random error in $\mathtt{M}_{nm}$. Let the value of the kth pixel be $s_k = P(p_k) + G(\sigma)$, where p_k is the mean photon count and σ is the read noise in rms. The expectation of the estimate $\hat{\mathtt{M}}_{nm}$ is given as,

$$\mathtt{E}\left[\hat{\mathtt{M}}_{nm}\right] = \mathtt{E}\left[\frac{\sum_k s_k \phi_{nm,k}}{\sum_k s_k}\right] = \mathtt{E}\left[\frac{A}{B}\right] = \mathtt{E}\left[A\right] \mathtt{E}\left[\frac{1}{B}\right] \approx \mathtt{M}_{nm}(1 + \mathtt{SNR}^{-2}), \tag{17}$$

where $\mathtt{SNR}^2 = (\sum_k p_k)^2 / \sum_k (p_k + \sigma^2)$. A and $1/B$ are assumed independent. The series expansion of $1/B$ up to order 2 is used to compute $\mathtt{E}\left[1/B\right]$. The variance of $\hat{\mathtt{M}}_{nm}$ is expressed as $\mathtt{var}\left[\hat{\mathtt{M}}_{nm}\right] = \mathtt{E}\left[A^2\right] \mathtt{E}\left[1/B^2\right] - \mathtt{E}\left[\hat{\mathtt{M}}_{nm}\right]^2$, where no correlation between A^2 and $1/B^2$ is assumed. Expanding $1/B^2$ as done for $1/B$ in Eq. 17 leads to

$$\mathtt{var}\left[\hat{\mathtt{M}}_{nm}\right] \approx \frac{\mathtt{M}_{nm}^2}{\mathtt{SNR}^2} + \frac{\sum_k p_k \phi_{nm,k}^2}{(\sum_k p_k)^2} + \frac{\sigma^2 \sum_k \phi_{nm,k}^2}{(\sum_k p_k)^2}. \tag{18}$$

The first term grows with the moment and is scaled by $1/\mathtt{SNR}^2$ (or $1/N_{ph}$). Since $\phi_{nm,k}^2 = x_k^{2n} y_k^{2m}$, the second term is essentially $\mathtt{M}_{2n2m}$ scaled by $1/N_{ph}$. For instance, the variance of $\mathtt{M}_{10}$ of a PSF with a finite width is given by $\mathtt{M}_{20}$, which is non-zero even if the PSF is perfectly centered. These two essentially depend on the intrinsic shape of the (unknown) PSF. The last term is due to $\sum_k \phi_{nm,k}^2 \propto N_{px} H^{2(n+m)}$, where H is a characteristic size of the PSF region (e.g. max. radius), scaled by σ^2/N_{ph}^2. For a PSF with fixed N_{px} (or resolution) and σ, this term follows a $1/N_{ph}^2$ trend and can dominate the other two terms especially at low $\mathtt{SNR}$. For a bright target at a high resolution, these terms could be estimated by substituting $\hat{\mathtt{M}}_{nm}$ and s_k for $\mathtt{M}_{nm}$ and p_k, respectively.

The error in Eq. 18 then propagates to the $q \times 1$ coefficient vector $\vec{c}$ of an order q polynomial fit to $\{\hat{\mathtt{M}}_{nm}\}$ measured at focus modulations $\{F_i,\, i = 1, 2, \cdots, K\}$ (Eq. 19).

$$\vec{c} = (\mathbf{A}^T \mathbf{A})^{-1} (\mathbf{A}^T \vec{b}) \text{ with } A_{ij} = \frac{F_i^j}{\mathtt{e}_i}\ ,\ b_i = \frac{\hat{\mathtt{M}}_{nm}^{(F_i)}}{\mathtt{e}_i}. \tag{19}$$

where $\vec{b}$ is the $K \times 1$ vector of $\{\hat{\mathtt{M}}_{nm}\}$, $\mathbf{A}$ is a $K \times q{+}1$ fit matrix, and $\mathtt{e}_i$ is the square root of $\mathtt{var}\left[\hat{\mathtt{M}}_{nm}\right]$ at F_i. c_q becomes the estimate of $d\mu_{nm}$. Letting $\mathbf{D} = (\mathbf{A}^T \mathbf{A})^{-1}$, D_{qq} becomes the error variance estimate of $d\mu_{nm}$[?] and propagates to $\vec{W}$ as,

$$\vec{W} = (\mathbf{B}^T \mathbf{B})^{-1} (\mathbf{B}^T \vec{d}) \text{ with } B_{ij} = \frac{M_{ij}}{\mathtt{v}_i}\ , d_i = \frac{u_i}{\mathtt{v}_i}, \tag{20}$$

where $\mathtt{v}_i$ is the square root of the error variance of u_i. Finally, by Letting $\mathbf{J} = (\mathbf{B}^T \mathbf{B})^{-1}$, J_{ii} becomes the error variance estimate of W_i. These error models have been validated via numerical simulations.[14]

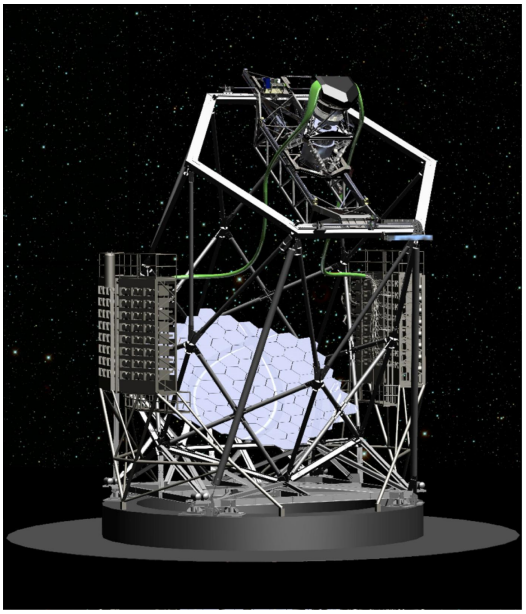

Figure 2. Rendering of the upgraded HET with the VIRUS instrument mounted on the side of the telescope.

4. MWFS FIELD APPLICATION TO THE VIRUS UNIT SPECTROGRAPHS

4.1 The VIRUS Instrument

The VIRUS instrument is made up of 150+ individually compact and identical spectrographs, each fed by a fiber integration field unit.[15,16] The instrument provides integral field spectroscopy from 350nm to 550nm of over 33,600 spatial elements per observation, each 1.8 sq. arc-seconds on the sky, at a spectral resolution of R 700. The instrument will be fed by a new wide-field corrector (WFC) of the Hobby-Eberly Telescope (HET) with increased science field of view as large as 22 arc-minutes in diameter and telescope aperture of 10m.[17]

The main science motivation of the VIRUS instrument is to map the evolution of dark energy for the Hobby-Eberly Telescope Dark Energy Experiment (HETDEX), by observing 0.8M Lyman-α emitting galaxies as tracers. In order to achieve this science objective, we are conducting three main engineering/science projects: a major telescope upgrade including replacing the top end of the telescope to allow for a larger focal plane (Wide Field Upgrade)[9], the construction of the Visual Integral-Field Replicable Unit Spectrograph (VIRUS) instrument, and the execution of a large area (5000 square degrees) blind survey for Lyman-α emitting galaxies at redshifts $z < 3.5$. The requirement to survey large areas of sky with the VIRUS instrument and the need to perform wavefront sensing for closed-loop active alignment control of the tracker position led us to design a new corrector employing meter-scale mirrors and covering a 22-arcmin diameter field of view. The HET Wide Field Upgrade (WFU) deploys this wide field corrector (WFC), a new tracker prime focus instrument package (PFIP), and new metrology systems. The new corrector has improved image quality and a 10m pupil diameter. The periphery of the field will be used for guiding and wavefront sensing to provide the necessary feedback to maintain the telescope alignment correctly. The WFC will give 30 times larger observing area than the current HET corrector. It is a four-mirror design with two concave 1 meter diameter mirrors, one concave 0.9 meter diameter mirror, and one convex 0.23 m diameter mirror. In order to feed optical fibers at f/3.65 to minimize focal ratio degradation (FRD), the WFC is designed to be telecentric at its curved focal surface so that the chief rays from all field angles are normal to the concave spherical focal surface centered at the exit pupil vertex. Due to excellent aberration correction, the imaging performance of the WFC is 0.5arcsec or better over the entire field of view with minimal obscuration across the field. The College of Optical Sciences at the University of Arizona is manufacturing the WFC. A new tracker is needed to accommodate the size and four-fold weight increase of the new PFIP. It will be a third generation evolution of the trackers for HET and SALT, and is in essence a precision six-axis motion control stage. The tracker is developed by the Center for Electro-Mechanics (CEM) at the University of Texas at Austin.[18]

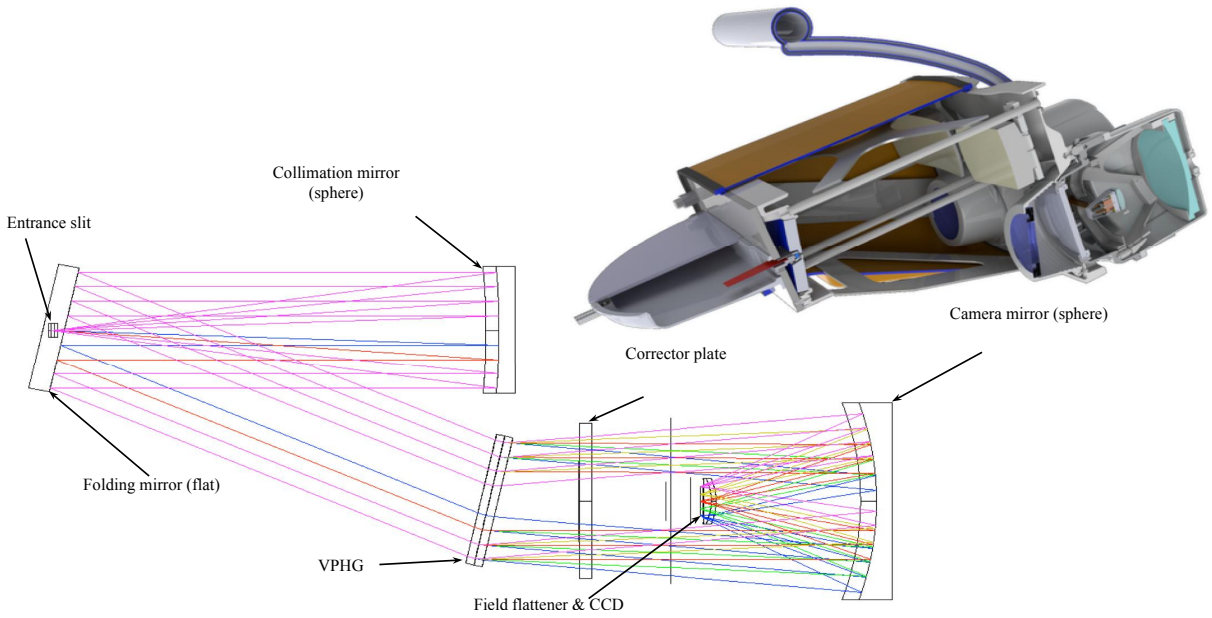

Figure 3. The optical layout and solid model of a VIRUS unit.

The VIRUS is based upon a novel instrument design philosophy unlike those used in traditional astronomical spectroscopic instrumentation where a monolithic single spectrograph for a large telescope with large and expensive optics and mechanisms observes the entire focal plane of the telescope. We have taken a different approach to designing the VIRUS instrument based on our concept and studies, where we concluded that industrial replication offers significant cost-advantages when compared to a traditional monolithic spectrograph, particularly in the cost of the optics and engineering effort. This concept appears to be a cost-effective approach to outfitting the existing large telescopes as well as the coming generation of ELTs, for certain instrument types, where the multiplex advantage can be used to image-slice and thus avoid growth in the scale of instruments with telescope aperture. This new approach led us to the VIRUS instrument design as follows. The entire VIRUS instrument is comprised of an array of simple, compact, inexpensive, and yet highly performing unit optical spectrographs. Each VIRUS unit samples only a small fraction of the telescope focal plane that is finely sampled by 224 fibers each covering 1.8arcsec^2 on the sky. The fibers feeding a two-unit module are packaged in a square array format that covers a 50x50arcsec^2 Integral Field Unit (IFU) with a 1/3 fill-factor. A three-exposure dither pattern fills in the gap. The optical design of the unit spectrograph is essentially based upon two Schmidt design; one as a collimator in a reversed Schmidt form and the other as a camera in a normal Schmidt design, both joined together at a common pupil plane. The optical beam train is formed by three reflections and four refractions (i.e. three mirrors and two lenses). With dielectric reflective coatings optimized for the wavelength range, high throughput is obtained. The full VIRUS array will consist of between 150 and 194 units, depending on funding, and simultaneously observe a minimum of 33,600 spectra with 12 million resolution elements. The IFUs are arrayed within the 22arcmin field of the upgraded HET with 1/7 fill factor, sufficient to detect the required density of LAEs for HETDEX. Development is proceeding with the prototype (VIRUS-P),[19] deployed in October 2006, and the production prototype where value engineering has been used to reduce the cost for production. Figure 2 shows a rendering of the upgraded telescope, showing the VIRUS mounted to the side of the telescope. The construction of the large number of VIRUS units requires the individual spectrographs be interchangeable at sub-system level and a production line assembly process be utilized, while meeting the optical performance specification. These requirements pose a strong emphasis on careful analysis of the manufacturing and alignment tolerances of the unit spectrograph design. Figure 3 illustrates the optical layout of the VIRUS unit spectrograph and a sectioned view of the two-unit VIRUS module opto-mechanical model. The optical design of the unit spectrograph is comprised of two sub-systems, both based upon the Schmidt design concept utilizing a Volume Phase Holographic Grating (VPHG). In-depth discussion about the design, tolerance, and construction of the instrument can be found elsewhere.[20]

4.2 Application Examples

To generate focus-modulated images, we moved the collimator mirror along the optical axis by adjusting three manual micrometers on the back of the mirror. We used five modulations per run and three image frames and three background frames are taken per modulation with exposure time of roughly 5 to 10 seconds per frame. Under the line lamp illumination, the fully exposed IFU creates closely packed images of the fiber slit. The fiber images are close to each other with about 1 pixel separation and they overlap with the adjacent ones when focus-modulated, making it impossible to determine the image moments of individual fiber images. Therefore we placed a mask at the input of the IFU so that only some of the fibers are exposed to the line lamp illumination, resulting in sparse fiber images across the slit dimension on the CCD. Since the line lamps create semi-discrete wavelengths, the resultant CCD image contains a grid of fiber images across the frame. This makes it ideal for computing the image moments of the fiber images at different focus-modulations.

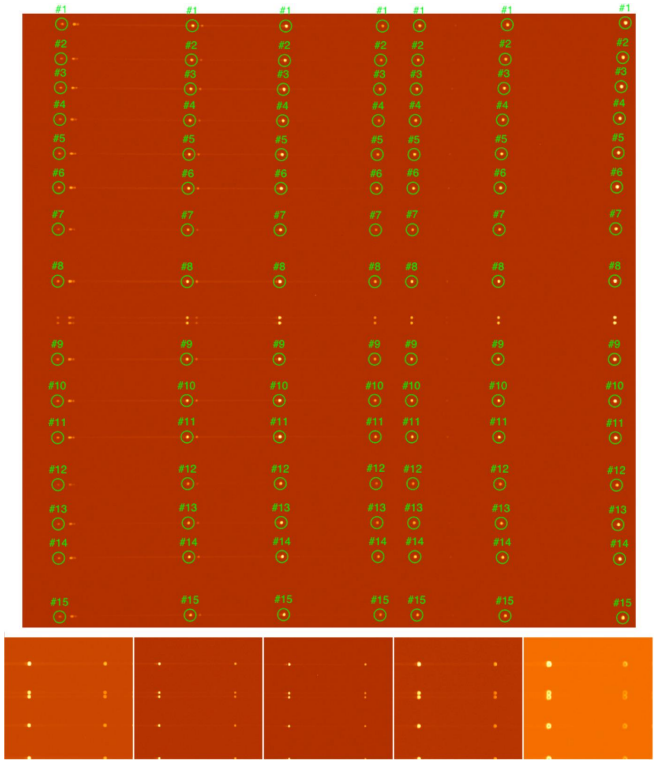

Figure 4. (Top) An example of fiber grid image, (Bottom) The close up of central section of image frames at 5 focus-modulations.

The acquired images are then processed through the MWFS pipeline software, where the modal coefficients associated with individual fiber images and their errors are estimated. Each estimated coefficient is then fitted by a quadratic curve across the slit or the wavelength dimension, resulting in the gradients of the coefficient in both directions across the CCD. The gradients are then used to determine the required tip and tilt angles of the camera mirror and/or the collimator mirror. For the defocus term, the zero-th order curve fit value provides the overall piston focus correction. We use the piston focus estimate only as a guidance and do not attempt to completely zero out the focus term because the zero defocus in fact results in slightly larger PSF. Therefore, the final focus adjustment is done by a combination of the visual inspection of the fiber images and then confirmed by the final contrast test. The adjustment from the pipeline software is then applied to the mirrors. We first apply the tip/tilt corrections to the mirrors by adjusting the micrometers on the collimator mirror and the dial adjusters on the camera mirror. Once the tip/tilt correction is complete, we apply the estimated piston focus correction followed by visual guidance. We then perform a follow-up modulation run to determine if the applied correction in the first run was successful and to see if there is any residual tip/tilt/focus corrections necessary.

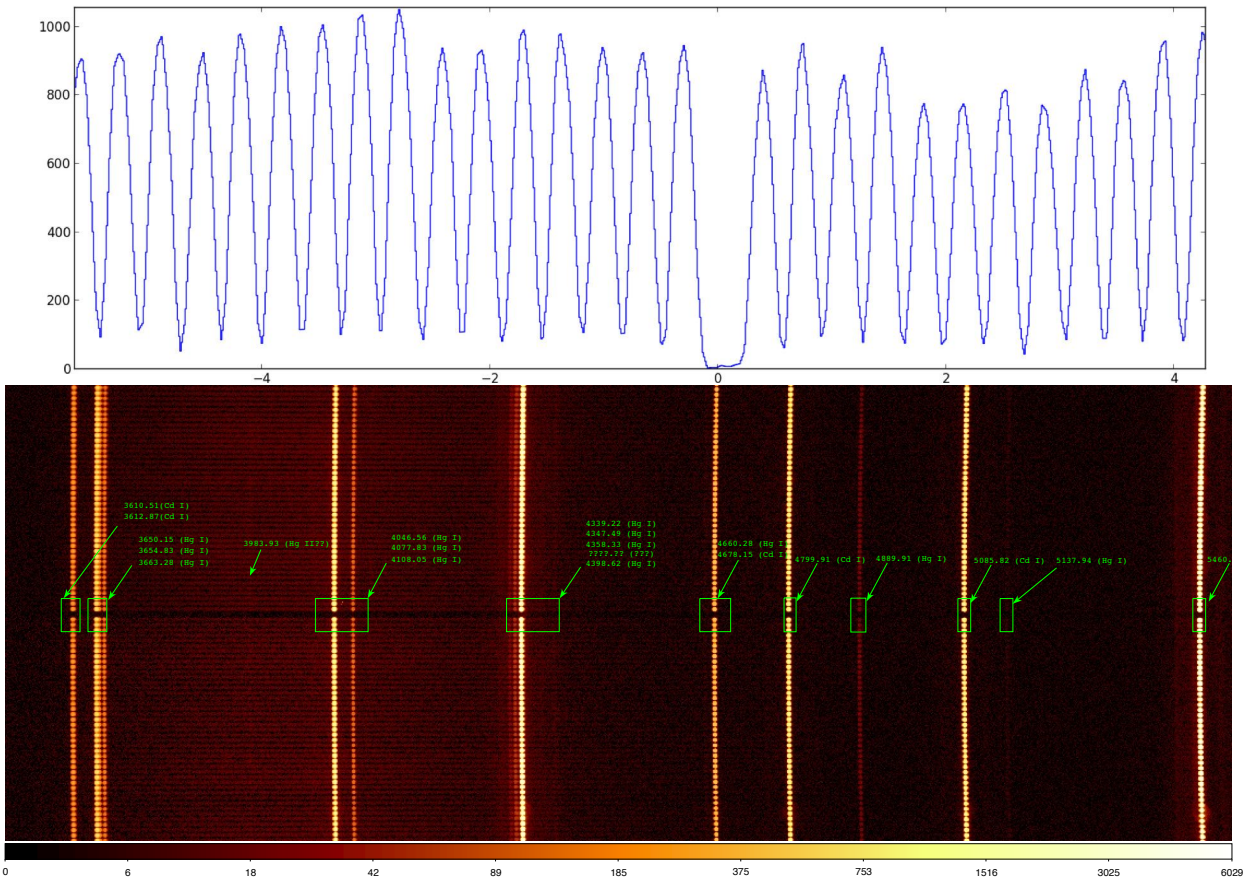

Figure 5. (Top) An example fiber slit image cross section used in the contrast test, (Bottom) The Hg+Cd lines across the CCD with each line wavelengths marked.

Note that, throughout the alignment of the VIRUS units so far, we typically needed two modulation runs and thus two corrections. After these corrections, we fine-tune the focus by the contrast test on the fully exposed IFU images without the IFU mask. In the contrast test, we slice through the centers of the fully exposed fiber images in the slit dimension and then compute the peak value of each fiber image and the valley value of between two fibers. We then compute the standard contrast of $(I_{peak} - I_{valley})/(I_{peak} + I_{valley})$ for each fiber image. The requirement is that 90 percent of the fiber images across the CCD must have the contrast value higher than 60 percent. This test gives a quite sensitive feedback on the focus adjustment.

Figure 6 shows the astigmatism and defocus terms of across the VIRUS unit #013 Channel-A CCD before and after the first correction. The first modulation run revealed that this channel had a substantial gradient in the spatial dimension. The top two plots (shown against the slit axis) show strongly tilted defocus and astigmatism. The bottom two plots (show against the wavelength axis) also show the same effect but in the orthogonal dimension, in that all red curves are quite flat in the spectral dimension, but widely separated from each other. In the same plots, the blue curves show the aberration terms measured in the second modulation run (i.e. after the first correction was made). It shows that the correction was effective and the aberration curves are gathered tightly together around the zero value. There is still small amount of residual gradient, but that can be tolerated. The corrected curves start showing the intrinsic field dependence in both spatial and spectral dimensions. The error bars are 3-σ value derived from the error propagation models described in Section 3.

As another example, Figure 7 shows the astigmatism and defocus terms of across the VIRUS unit #023 Channel-A CCD before and after the first correction. Unlike #013-A, this channel shows more substantial gradient in the spectral dimension than in the spatial axis. The distribution pattern of the red curves are the same as in #013-A, but along the opposite axis. After the first correction, the blue curves gather together

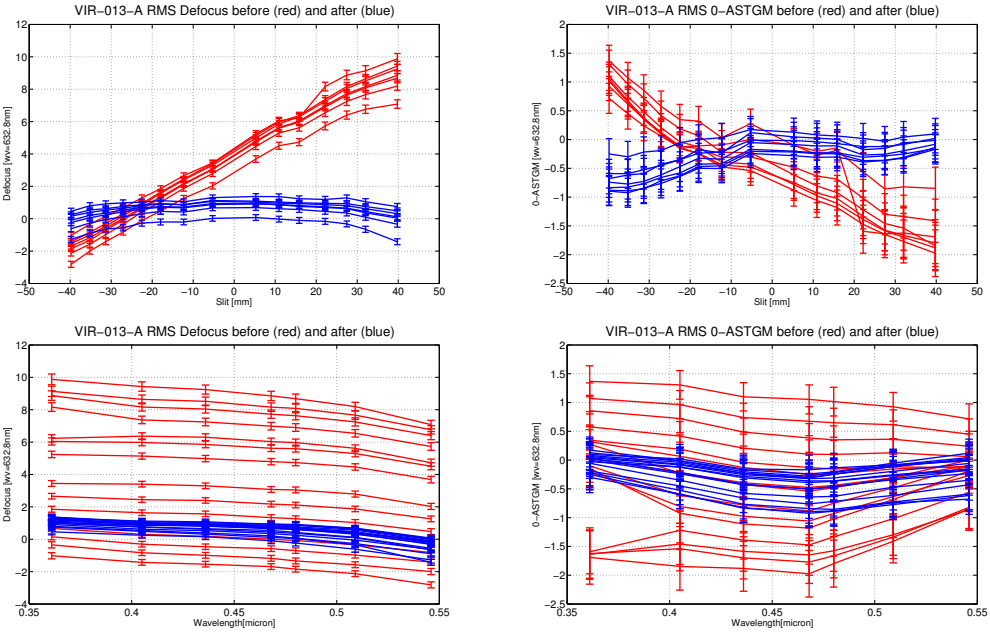

Figure 6. (Top left) Defocus term plotted in the slit dimension, (Top right) 0-degree Astigmatism term plotted in the slit dimension, (Bottom left) Defocus term plotted in the wavelength dimension, (Bottom right) 0-degree Astigmatism term plotted in the wavelength dimension. Note that the red curves are before the first correction and the blue curves are after correction. The individual curves in the same color represents different wavelengths for the top row plots and different slit positions for the bottom row plots.

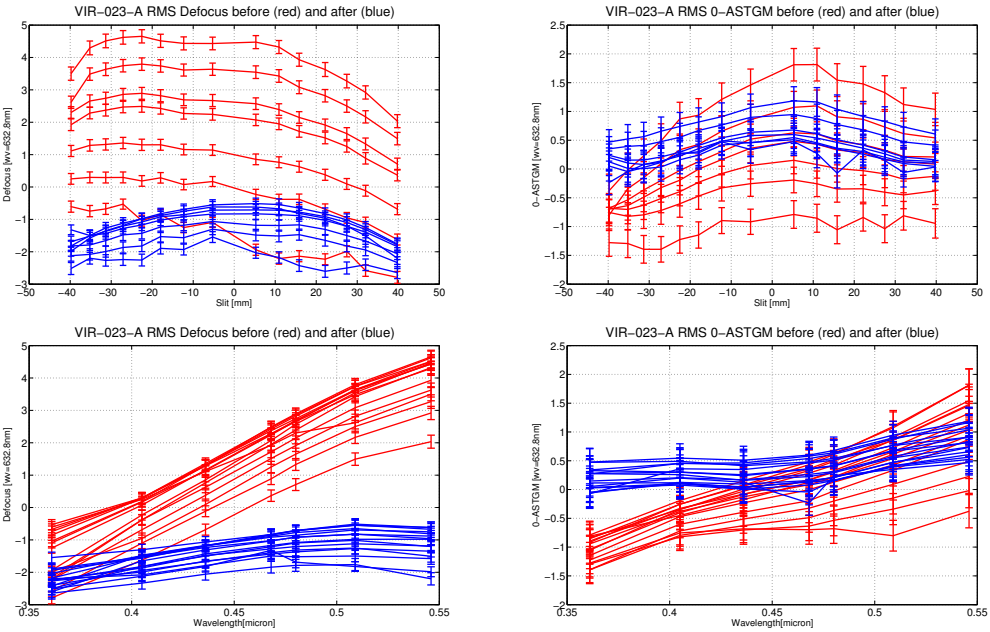

Figure 7. (Top left) Defocus term plotted in the slit dimension, (Top right) 0-degree Astigmatism term plotted in the slit dimension, (Bottom left) Defocus term plotted in the wavelength dimension, (Bottom right) 0-degree Astigmatism term plotted in the wavelength dimension. Note that the red curves are before the first correction and the blue curves are after correction. The individual curves in the same color represents different wavelengths for the top row plots and different slit positions for the bottom row plots.

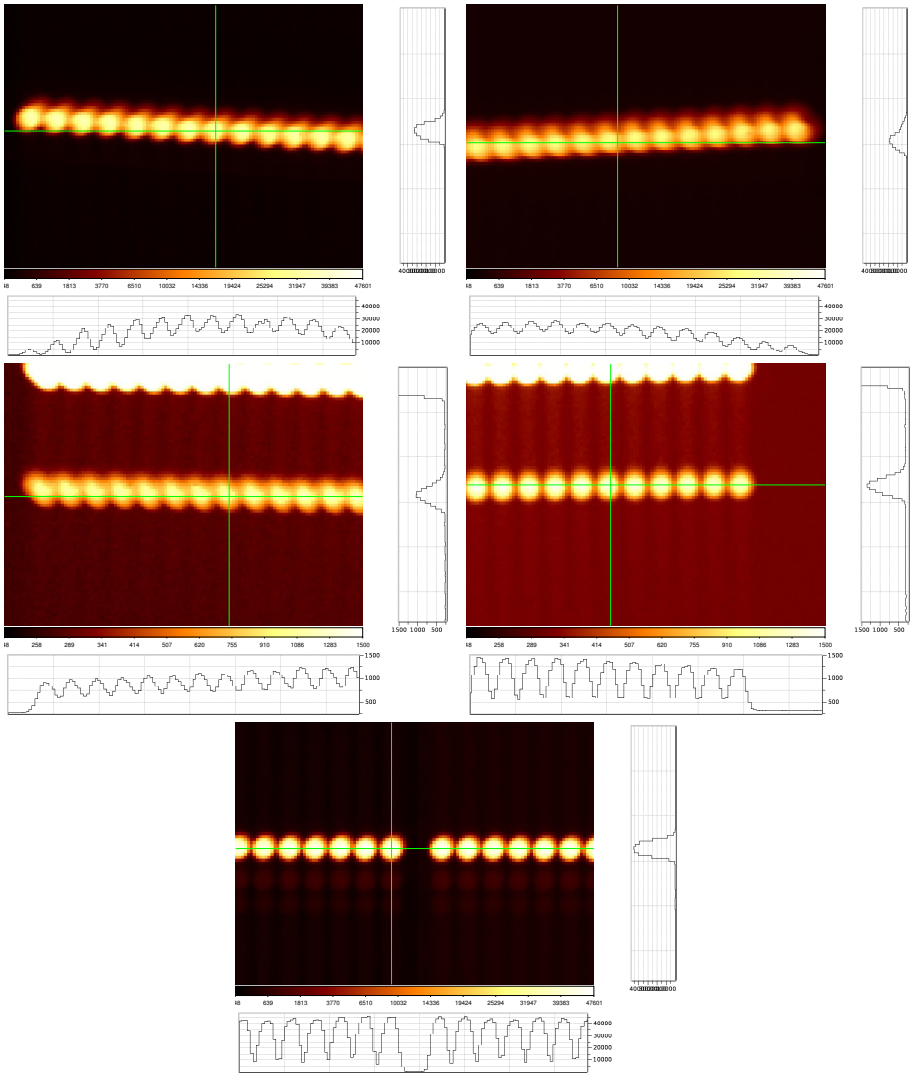

Figure 8. (Top left) Initial fiber images in top-left corner of the CCD at 546nm, (Top right) in top-right corner of the CCD at 546nm, (Middle left) bottom-left corner of the CCD at 361nm, (Middle right) bottom-right corner of the CCD at 361nm, and (bottom) center of the CCD at 436nm.

tightly and the spectral gradient is mostly gone. This channel shows more piston focus error (about 1.5wv) than #013-A (about 0.5wv). As discussed earlier, these values are not completely zeroed out. Instead, they provide the direction of focus correction and the focus tuning is done visually. The last fine focus tuning and verification are done by the contrast test.

Figure 8 shows the initial fiber images in various sections of the CCD. It is evident that the fiber images exhibit strong comatic tails as well as significant enlarged size that are dependent of the locations on the CCD. After all fine alignment processes, the fiber images show very tightly focused without comatic tails (Figure 9). Note that the fiber images at 361nm (middle row) show a little bit of tail-like spread. As indicated in Figure 5, this is due to two unresolved wavelengths (361.05nm and 361.29nm). Such phenomena appear throughout the CCD for different lines. There is also the final contrast distribution plot. It shows what fraction of fiber images across the CCD is above a certain contrast ratio. As mentioned earlier, the requirement is that 90% of fiber images need to have contrast higher than 60%. This requirement is met in this particular channel.

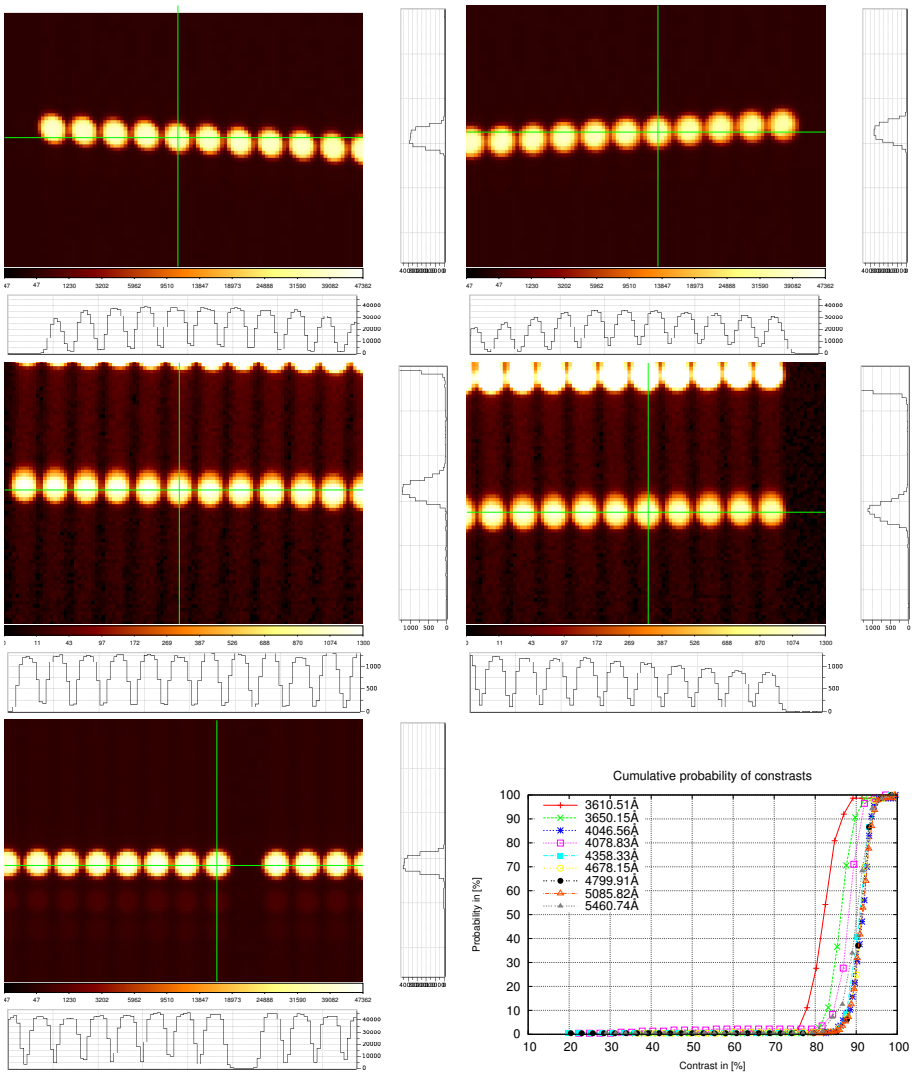

Figure 9. (Top left) Final fiber images in top-left corner of the CCD at 546nm, (Top right) in top-right corner of the CCD at 546nm, (Middle left) bottom-left corner of the CCD at 361nm, (Middle right) bottom-right corner of the CCD at 361nm, and (bottom-left) center of the CCD at 436nm. (Bottom-right) Final contrast distribution across the CCD.

4.3 Fine alignment statistics and efficiency analysis

There are more than 29 VIRUS units (58 channels) have been assembled and aligned so far. To check how efficiently the alignment process has been done, we derived some statistics of various parameters across the 58 channels as show in Figure 10. The gradient and tip/tilt values are 1-σ variation of those values across the channels after the first correction (since we do not run a focus modulation after the second correction). For both channels, the defocus gradient correction in the spatial direction appears excellent. The reduction in the spectral gradient is x2 for channel A and x8 for channel B. The tilt adjustment required after the first correction follows a similar trend. To compute the spatial plate scale error, we first compute the separation between two edge fiber images at 436nm line, which is roughly at the center of the CCD. We then take the difference of this from the Zemax model value at the same wavelength. The difference is then divided by the model distance between the fiber images. For the spectral gross plate scale, we did the same thing but for the two extreme wavelength images of one of the two center fibers. The spectra positioning error comes from the standard deviation of the centroid of one of the two center fibers at 436nm line. The requirement is 6.5 pixels. Finally, the contrast pass rate is just the fraction of channels that have passed the final contrast test. The reason why B is less than 100% is because

one of the B channels was not completed aligned due to the detector shadow issue that we encountered. This result indicates that we have been able to compensate for the alignment errors quite effectively. This is reflected in the fact that only two modulation runs are typical for aligning one channel. We could add another modulation run to check the final status of the field aberration distribution. However, this adds rather unnecessary overhead to the alignment process since the final image quality is directly confirmed by the contrast test. It takes roughly a couple hours to complete two modulation runs as well as follow-up measurement/manual adjustment. There are other alignment activities like grating rotation and plate-scale correction and the final contrast test. Including these and the mirror locking/verification steps, the total time required is roughly a half day per channel. Since the unit needs to be cooled and pumped down before the alignment starts and warmed and pumped up after the alignment, this adds about 3 days of overhead time to the overall process. Currently, the rate of alignment is about 1.5 units over two weeks, which will ensure the full complement of the VIRUS units be completed around the end of the year.

	CHANNEL A		CHANNEL B		
METRIC	BEFORE	AFTER	BEFORE	AFTER	UNIT
Defocus spatial gradient	0.039	0.005	0.064	0.007	wv/mm
0-Astg. spectral gradient	10.564	4.412	6.663	2.011	wv/um
COL Spatial tilt comp	0.117	0.014	0.217	0.079	degree
CAM Spatial tilt comp	0.118	0.015	0.224	0.082	degree
COL Spectral tilt comp	0.242	0.099	0.141	0.042	degree
CAM Spectral tilt comp	0.254	0.105	0.147	0.045	degree
Spatial plate scale error	n/a	0.090	n/a	0.050	%
Spectral gross dispersion error	n/a	0.100	n/a	0.100	%
Spectra positioning error	n/a	less than 4	n/a	less than 3	pixel
Constrast pass rate	0	100	0	98	%

Figure 10. Fine optical alignment statistics and efficiency analysis.

5. CONCLUSION

In this paper, we detailed the technical update/progress (mainly the error propagation analysis) made so far for the moment-based wavefront sensing method and the statistical estimates of the before/after alignment aberrations, image-quality, and various efficiency indicators of the unit spectrograph alignment process. We revisited the basic theory of the MWFS and then laid out the update on the error propagation analysis in terms of the pixelation error, photon noise, and read-out noise in Section. We described the application to the VIRUS instrument alignment with two example cases of VIRUS unit #013-A and #023-A. The fine optical alignment statistics and efficiency analysis is given. In one alignment correction, the procedure efficiently reduced the overall image gradients in both spatial and spectral dimensions. The substantial fraction of VIRUS channels has passed the final contrast test. Including all overheads, the alignment rate is 1.5 units over two weeks, which will ensure the full complement of the VIRUS units be completed around the end of the year.

ACKNOWLEDGMENTS

HETDEX is run by the University of Texas at Austin McDonald Observatory and Department of Astronomy with participation from the Ludwig-Maximilians-Universitt München, Max-Planck-Institut fr Extraterrestriche-Physik (MPE), Leibniz-Institut für Astrophysik Potsdam (AIP), Texas A&M University, Pennsylvania State University, Institut für Astrophysik Göttingen, University of Oxford and Max-Planck-Institut für Astrophysik (MPA). In addition to Institutional support, HETDEX is funded by the National Science Foundation (grant AST-0926815), the State of Texas, the US Air Force (AFRL FA9451 -04-2-0355), and generous support from private individuals and foundations.

REFERENCES

[1] Suiter, H. R., [*Star Testing Astronomical Telescopes*], Willmann-Bell (2008 (2nd Ed.)).

[2] Fienup, J. R., "Phase retrieval algorithms: a comparison," *Appl. Opt.* **21**, 2758–2769 (1982).

[3] Roddier, F., "Wavefront sensing and the irradiance transport equation," *Appl. Opt.* **29**, 1402 (1990).

[4] Hardy, J. W., [*Adaptive Optics in Astronomical Telescopes*], Oxford (1988).

[5] Gonsalves, R., "Small-phase solution to the phase-retrieval problem," *Opt. Lett.* **26**, 684–685 (2001).

[6] Keller, C. U., Korkiakoski, V., Doelman, N., Fraange, R., Andrei, R., and Verhaegen, M., "Extremely fast focal-plane wavefront sensing for extreme adaptive optics," in [*Astronomical Telescopes and Instrumentation*], Loew, M. H., ed., *Proc. SPIE* **8447**, 844721–1 (2012).

[7] Dolne, J., Menicucci, P., Miccolis, D., Widen, K., Seiden, H., Vachss, F., and Schall, H., "Advanced image processing and wavefront sensing with real-time phase diversity," *Appl. Opt.* **48**, A30–A34 (2009).

[8] Meimon, S., Fusco, T., and Mugnier, L., "Lift: A focal-plane wavefront sensor for real-time low-order sensing on faint sources," *Opt. Lett.*. **35**, 3036–3038 (2010).

[9] Teague, M. R., "Irradiance moments: their propagation and use for unique retrieval of phase," *J. Opt. Sci. Am.* **72**, 1199–1209 (1982).

[10] Lee, H., "Modal analysis of focus-diverse point spread functions for modal wavefront sensing of uniformly illuminated circular-pupil systems," *Opt. Lett.* **36**, 1503–1505 (2011).

[11] Lee, H. and Hill, G. J., "Image moment-based wavefront sensing for in-situ full-field image quality assessment," in [*Astronomical Telescopes and Instrumentation*], Loew, M. H., ed., *Proc. SPIE* **8450**, 845019–1 (2012).

[12] Lee, H., Hill, G. J., Tuttle, S. E., and Vattiat, B. L., "Fine optical alignment correction of astronomical spectrograph via in-situ full-field moment-based wavefront sensing," in [*Astronomical Telescopes and Instrumentation*], Loew, M. H., ed., *Proc. SPIE* **8450**, 845019–2 (2012).

[13] Noll, R. J., "Zernike polynomials and atmospheric turbulence," *J. Opt. Soc. Am.* **66**, 207 (1976).

[14] Lee, H., "Error analysis of moment-based modal wavefront sensing," *Opt. Lett.* **39**, 1286–1389 (2014).

[15] Hill, G. et al., "Virus: Production and deployment of a massively replicated fiber integral field spectrograph for the upgraded hobby-eberly telescope," in [*Astronomical Telescopes and Instrumentation*], *Proc. SPIE* **9147**, 9147–25 (2014).

[16] Tuttle, S. et al., "The construction, alignment, and installation of the virus spectrograph," in [*Astronomical Telescopes and Instrumentation*], *Proc. SPIE* **9147**, 9147–26 (2014).

[17] Hill, G. et al., "Deployment of the hobby-eberly telescope wide field upgrade," in [*Astronomical Telescopes and Instrumentation*], *Proc. SPIE* **9145**, 9145–5 (2014).

[18] Good, J. et al., "Design of performance verification testing for het wide-field upgrade tracker in the laboratory," in [*Astronomical Telescopes and Instrumentation*], *Proc. SPIE* **7739**, 7739–152 (2010).

[19] Hill, G. J. et al., "Design, construction, and performance of virus-p: the prototype of a highly replicated integral-field spectrograph for het," in [*Astronomical Telescopes and Instrumentation*], *Proc. SPIE* **7014**, 7014–257 (2008).

[20] Lee, H. et al., "Virus optical tolerance and production," in [*Astronomical Telescopes and Instrumentation*], *Proc. SPIE* **7735**, 7735–140 (2010).